






Three-dimensional Ising ferrimagnetism of Cr-Fe-Cr trimers in FeCr₂Te₄Yu Liu (刘育)¹, R. J. Koch¹, Zhixiang Hu (胡之翔)^{1,2}, Niraj Aryal,¹ Eli Stavitski,³ Xiao Tong (佟晓)⁴, Klaus Attenkofer,³ E. S. Bozin¹, Weiguo Yin (尹卫国)¹ and C. Petrovic^{1,2}¹Condensed Matter Physics and Materials Science Department, Brookhaven National Laboratory, Upton, New York 11973, USA²Department of Materials Science and Chemical Engineering, Stony Brook University, Stony Brook, New York 11790, USA³National Synchrotron Light Source II, Brookhaven National Laboratory, Upton, New York 11973, USA⁴Center for Functional Nanomaterials, Brookhaven National Laboratory, Upton, New York 11973, USA

(Received 23 May 2020; accepted 18 August 2020; published 31 August 2020)

We carried out a comprehensive study of magnetic critical behavior in single crystals of ternary chalcogenide FeCr₂Te₄ that undergoes a ferrimagnetic transition below $T_c \sim 123$ K. Detailed critical behavior analysis and scaled magnetic entropy change indicate a second-order ferrimagnetic transition. Critical exponents $\beta = 0.30(1)$ with $T_c = 122.4(5)$ K, $\gamma = 1.22(1)$ with $T_c = 122.8(1)$ K, and $\delta = 4.24(2)$ at $T_c \sim 123$ K suggest that the spins approach the three-dimensional Ising ($\beta = 0.325$, $\gamma = 1.24$, and $\delta = 4.82$) model coupled with attractive long-range interactions between spins that decay as $J(r) \approx r^{-4.88}$. Our results suggest that the ferrimagnetism in FeCr₂Te₄ is due to itinerant ferromagnetism among the antiferromagnetically coupled Cr-Fe-Cr trimers.

DOI: [10.1103/PhysRevB.102.085158](https://doi.org/10.1103/PhysRevB.102.085158)**I. INTRODUCTION**

Ternary ACr₂X₄ (A = transition metal, X = S, Se, and Te) exhibits a variety of magnetic and electronic properties. The family includes metallic CuCr₂X₄ and semiconducting Hg(Cd)Cr₂Se₄ ferromagnets [1–3], semiconducting Fe(Mn)Cr₂S₄ ferrimagnets [4–6], and the insulating ZnCr₂S₄ antiferromagnet [7]. The FeCr₂X₄ compounds show competing spin-orbit and exchange interactions [8]. FeCr₂S₄ is a ferrimagnetic (FIM) insulator below $T_c = 165$ K and shows a crossover transition from insulator to metal near T_c and colossal magnetoresistance behavior [9–11]. FeCr₂Se₄ is an insulating antiferromagnet (AFM) with $T_N = 218$ K and ferrimagnetic with a small magnetic moment of $0.007\mu_B$ below 75 K [12–14]. It should be noted that FeCr₂Se₄ crystallizes in the Cr₃S₄-type monoclinic structure described within the $C2/m$ space group, in contrast to the cubic spinel type of FeCr₂S₄. However, FeCr₂S₄ and FeCr₂Se₄ have a similar electronic structure with nearly trivalent Cr³⁺ and divalent Fe²⁺ states [15]. The magnetic moments of Cr ions are antiparallel to those of Fe ions in FeCr₂X₄, and there is strong hybridization between Fe $3d$ states and X p states [15].

FeCr₂Te₄ has not been studied much, presumably due to the difficulty in sample preparation [16–18]. Demeaux *et al.* first grew the single crystals of FeCr₂Te₄ [16]. The crystal structure was reported as a defective NiAs type within the $P6_3/mmc$ space group, where Fe and Cr occupy the same site with an alloying ratio of 1:2 and a net occupancy of 0.75 [16]. In contrast, Valiev *et al.* reported that FeCr₂Te₄ crystallizes in a CoMo₂S₄-type structure within the $I2/m$ space group, in which Fe and Cr are octahedrally coordinated by six Te [17]. Recently, a series of polycrystals FeCr₂Se_{4-x}Te_x were synthesized [18]. Substitution with Te gradually suppresses the AFM order of FeCr₂Se₄ and leads to a short-range ferromagnetic (FM) cluster metallic state in polycrystal FeCr₂Te₄ [18]. In

order to study the intrinsic physical property, high-quality single crystal is required.

In this work, we successfully fabricated single crystals of FeCr₂Te₄ and performed a comprehensive study of the structural and magnetic properties. Our analysis of criticality around T_c indicates that FeCr₂Te₄ displays the three-dimensional (3D) Ising behavior, with the magnetic exchange distance decaying as $J(r) \approx r^{-4.88}$. Our first-principles calculations suggest that the ferrimagnetism in FeCr₂Te₄ stems from the itinerant ferromagnetism among the antiferromagnetically coupled Cr-Fe-Cr trimers. Since transition-metal chalcogenides represent model systems for exploring the local structure-related relationship between the broken symmetry and d -orbital magnetism [19], detailed local structure investigation of this system would be highly desirable and would bring important new insights.

II. EXPERIMENTAL DETAILS

Single crystals of FeCr₂Te₄ were fabricated by melting a stoichiometric mixture of Fe (99.99%, Alfa Aesar) powder, Cr (99.95%, Alfa Aesar) powder, and Te (99.9999%, Alfa Aesar) pieces. The starting materials were vacuum sealed in a quartz tube, heated to 1200 °C over 12 h, slowly cooled to 900 °C at a slow rate of 1 °C/h, and then quenched in ice water. The single crystal x-ray diffraction (XRD) data were taken with Cu $K\alpha$ ($\lambda = 0.15418$ nm) radiation of a Rigaku Miniflex powder diffractometer. In order to obtain more comprehensive crystallographic information, the powder XRD measurements were performed at the PDF beamline (28-ID-1) at National Synchrotron Light Source II (NSLS II) at Brookhaven National Laboratory (BNL) using a Perkin Elmer image plate detector. The setup utilized an x-ray beam with a wavelength of 0.1666 Å and a sample to detector distance of 1.25 m, as calibrated using a Ni standard. The sample was cooled

with an Oxford Cryosystems 700 cryostream using liquid nitrogen. Raw data were integrated and converted to intensity vs scattering angle using the software PYFAI [20]. The average structure was assessed from raw powder diffraction data using the General Structure Analysis System II (GSAS-II) software package [21]. The elemental analysis was performed using energy-dispersive x-ray spectroscopy (EDS) in a JEOL LSM-6500 scanning electron microscope. The x-ray absorption spectroscopy (XAS) measurements were performed at the 8-ID beamline of NSLS II (BNL) in a fluorescence mode. The x-ray absorption near-edge structure (XANES) and extended x-ray absorption fine structure (EXAFS) spectra were processed using the ATHENA software package. The AUTOBK code was used to normalize the absorption coefficient and separate the EXAFS signal $\chi(k)$ from the atom-absorption background. The extracted EXAFS signal $\chi(k)$ was weighed by k^2 to emphasize the high-energy oscillation and then Fourier transformed in a k range from 2 to 10 \AA^{-1} to analyze the data in R space. The x-ray photoelectron spectroscopy (XPS) experiment was carried out in an ultrahigh-vacuum system with base pressures $<5 \times 10^{-9}$ Torr, equipped with a hemispherical electron energy analyzer (SPECS, PHOIBOS 100) and a twin-anode x-ray source (SPECS, XR50). Al $K\alpha$ (1486 eV) radiation was used at 13 kV and 30 mA. The angle between the analyzer and the x-ray source was 45° , and photoelectrons were collected along the sample surface normal. The XPS spectra were analyzed and deconvoluted using the CASAXPS software. The dc and ac magnetic susceptibilities were measured in a Quantum Design MPMS-XL5 system. The applied field H_a was corrected as $H = H_a - NM$, where M is the measured magnetization and N is the demagnetization factor. The corrected H was used for the analysis of magnetic entropy change and critical behavior.

III. RESULTS AND DISCUSSION

In the single-crystal XRD pattern (inset in Fig. 1), only $(00l)$ peaks were observed. The synchrotron powder XRD pattern of pulverized crystal of FeCr_2Te_4 can be well fitted by using a monoclinic structure with the $I2/m$ space group (Fig. 1), confirming the main phase of FeCr_2Te_4 with less than 4% FeTe impurity. The determined lattice parameters at 300 K are $a = 6.822(2)$ \AA , $b = 3.938(1)$ \AA , $c = 11.983(5)$ \AA , and $\beta = 90.00(5)^\circ$, close to the reported values [17,18]. No structural transition was observed on cooling, showing a compression along the c axis with $c = 11.867(5)$ \AA and a slight expansion in the ab plane with $a = 6.825(1)$ \AA and $b = 3.943(1)$ \AA down to 105 K (Table I).

The ratio of elements in the single crystal as determined by EDS is Fe:Cr:Te = 0.99(2):1.90(2):4.0(1) [Fig. 2(a)], and it is referred to as FeCr_2Te_4 throughout this paper. The information on the valence states of Fe, Cr, and Te atoms can be obtained from the element core-level XPS spectra [Fig. 2(b)]: Fe^{2+} ($2p_{3/2} \sim 710$ eV, $2p_{1/2} \sim 723$ eV), Cr^{3+} ($2p_{3/2} \sim 575$ eV, $2p_{1/2} \sim 586$ eV), Te^{2-} ($3d_{5/2} \sim 572$ eV, $3d_{3/2} \sim 583$ eV). Figure 1(c) shows the normalized Cr and Fe K -edge XANES spectra, in which a similar prepeak feature is observed, indicating a similar local atomic environment for Fe and Cr atoms. The prepeak feature for the Fe K edge is somewhat weaker than that of the Cr K edge, suggesting a

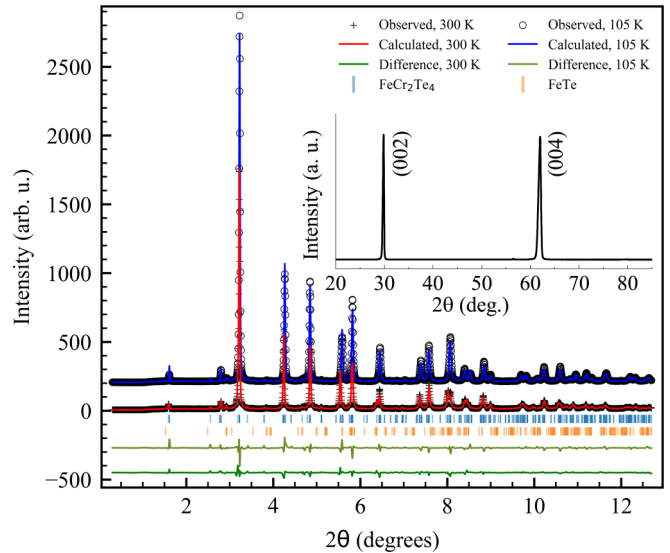


FIG. 1. Synchrotron powder x-ray diffraction (XRD) data and structural model refinements. The data are shown by + and \circ ; structural model fits at 300 and 105 K are shown by red and blue solid lines, respectively. The difference curves are given by green solid lines, offset for clarity. The vertical tick marks represent Bragg reflections of the $I2/m$ space group and up to 4% of FeTe impurity. The inset shows the single-crystal XRD pattern of FeCr_2Te_4 at room temperature.

weaker lattice distortion in FeTe_6 when compared with CrTe_6 . The edge features are close to the standard compounds with Cr^{3+} and Fe^{2+} oxidation states [22,23], in line with the XPS result.

The local environment of Fe and Cr atoms is revealed in the EXAFS spectra of FeCr_2Te_4 measured at room temperature

TABLE I. Average and local structural parameters extracted from the powder XRD and the EXAFS spectra of FeCr_2Te_4 . CN is the coordination number based on the crystallographic value, R is the interatomic distance, and σ^2 is the Debye-Waller factor.

		300 K	105 K		
a (\AA)		6.822(2)	6.825(1)		
b (\AA)		3.938(1)	3.943(1)		
c (\AA)		11.983(5)	11.867(5)		
β ($^\circ$)		90.00(5)	90.01(15)		
Atom	Site	x	y	z	
Fe	$2a$	0	0	0	
Cr	$4i$	0.001(3)	0	0.2541(8)	
Te1	$4i$	0.328(4)	0	0.3726(4)	
Te2	$4i$	0.339(4)	0	0.8785(4)	
Bond	CN	R (\AA)	ΔR (\AA)	σ^2 (\AA^2)	
Cr-Te1	2	2.58	0.01	0.001	
Cr-Te2	1	2.67	0.01	0.001	
Cr-Te3	1	2.80	0.11	0.003	
Cr-Te4	2	2.86	0.11	0.003	
Fe-Te1	4	2.69	0.36	0.02	
Fe-Te2	2	2.75	0.24	0.02	

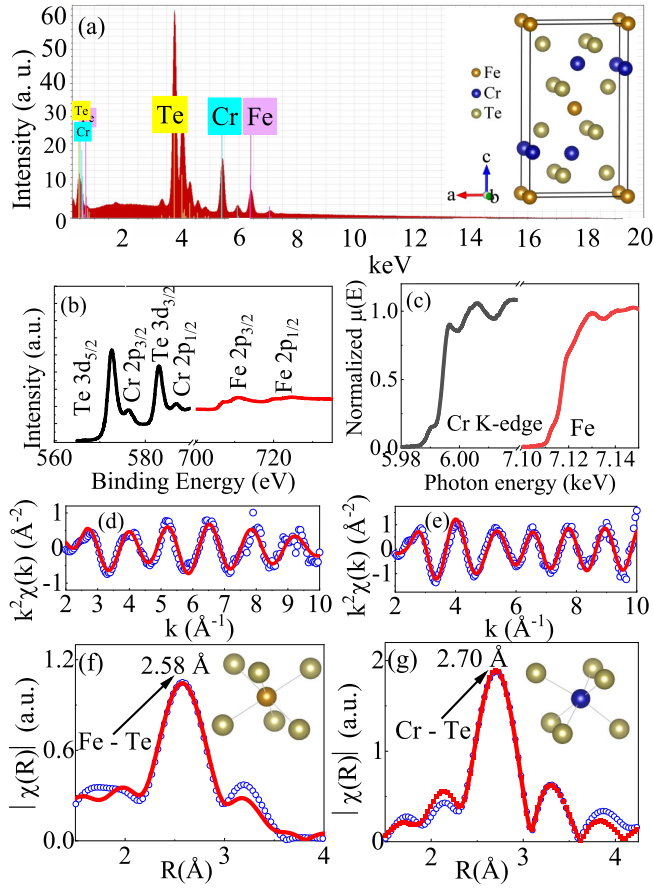


FIG. 2. (a) Crystal structure and results of EDS analysis on FeCr_2Te_4 . (b) Room-temperature Fe 2p, Cr 2p, and Te 3d core-level XPS and (c) normalized Cr and Fe K-edge XANES spectra. (d) and (e) Fe and Cr K-edge EXAFS oscillations and (f) and (g) Fourier transform magnitudes of EXAFS data measured at room temperature. The experimental data are shown as blue symbols alongside the model fit plotted as a red line. The corresponding first coordination shells of Fe and Cr are shown in the insets.

[Figs. 1(d) and 2(e)]. In a single-scattering approximation, the EXAFS can be described by [24]

$$\chi(k) = \sum_i \frac{N_i S_0^2}{k R_i^2} f_i(k, R_i) e^{-\frac{2R_i}{\lambda}} e^{-2k^2 \sigma_i^2} \sin[2kR_i + \delta_i(k)],$$

where N_i is the number of neighboring atoms at a distance R_i from the photoabsorbing atom. S_0^2 is the passive electron reduction factor, $f_i(k, R_i)$ is the backscattering amplitude, λ is the photoelectron mean free path, δ_i is the phase shift, and σ_i^2 is the correlated Debye-Waller factor measuring the mean-square relative displacement of the photoabsorber-backscatterer pairs. The corrected main peak in the Fourier transform magnitudes of Fe K-edge EXAFS around $R \sim 2.58 \text{ \AA}$ is clearly smaller than that of Cr K-edge EXAFS at $R \sim 2.70 \text{ \AA}$ [Figs. 1(f) and 2(g)]. The different local Fe-Te and Cr-Te bond lengths suggest that the Fe and Cr atoms might occupy different crystallographic sites, ruling out the possibility of a NiAs-type structure with the same Fe/Cr sites. Then we focus on the first-nearest neighbors of Fe and Cr atoms ranging from 1.5 to 3.5 \AA . The main peak corresponds to two Fe-Te bond

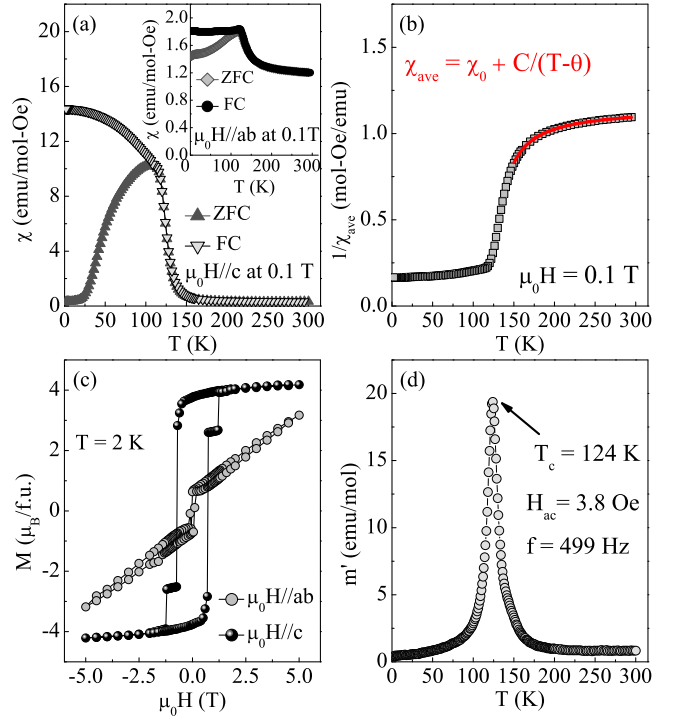


FIG. 3. (a) Temperature-dependent dc magnetic susceptibility $\chi(T)$ in zero-field cooling (ZFC) and field-cooling (FC) modes taken at $\mu_0 H = 0.1 \text{ T}$ for $\mu_0 \mathbf{H} \parallel \mathbf{c}$ and $\mu_0 \mathbf{H} \parallel \mathbf{ab}$ (inset), respectively. (b) $1/\chi(T)$ taken at $\mu_0 H = 0.1 \text{ T}$ along with the Curie-Weiss fit from 150 to 300 K. (c) Field dependence of magnetization for FeCr_2Te_4 measured at $T = 2 \text{ K}$. (d) The ac susceptibility real part $m'(T)$ measured with an oscillating ac field of 3.8 Oe and frequency of 499 Hz. The chosen experimental parameters (field and frequency) allow for a well-defined moment and adequate frequency resolution.

lengths of 2.69 and 2.75 \AA and four different Cr-Te bond lengths with 2.58, 2.67, and 2.80, and 2.86 \AA , extracted from the model fits with a fixed coordination number. The peaks above 3.25 \AA are due to longer Fe-Cr, Fe-Te, and Cr-Te bond distances, and the multiple scattering involving different near neighbors of the Fe/Cr atoms.

Figure 3(a) shows the temperature dependence of magnetization measured in out-of-plane field $\mu_0 H = 0.1 \text{ T}$, in which χ increases with decreasing temperature and increases abruptly near T_c due to the paramagnetic (PM)-FIM transition. The in-plane $\chi(T)$ [inset in Fig. 3(a)] is much smaller than that in the out-of-plane field, indicating the presence of large magnetic anisotropy with an easy c axis. The average susceptibility $\chi_{\text{ave}} = (2/3)\chi_{ab} + (1/3)\chi_c$ from 150 to 300 K can be fitted by the Curie-Weiss law $\chi_{\text{ave}} = \chi_0 + C/(T - \theta)$ [Fig. 3(c)], which yields $\chi_0 = 0.87(1) \text{ emu/mol Oe}$, $C = 7.91(6) \text{ emu K/mol Oe}$ [$\mu_{\text{eff}} = 7.95(9)\mu_B$ per formula unit], and $\theta = 126.6(2) \text{ K}$. The positive value of θ indicates the dominance of ferromagnetic or ferrimagnetic exchange interactions in FeCr_2Te_4 . For monoclinic FeCr_2Se_4 with a similar layered structure, the individual spins of Fe and Cr ions have AFM coupling along the c axis with a distance of 2.956 \AA , while FM coupling is along the b axis with a distance of 3.617 \AA [25]. At low temperature, the FM interaction dominating over the AFM interaction results in a

FIM ground state. For FeCr_2Te_4 , the enhanced hybridization between the d orbital of Fe and Cr with the p orbital of Te plays an important role in magnetic coupling. Based on our first-principles calculation (see below), the FIM structure where Fe and Cr atoms have opposite spin orientations is the most stable state in FeCr_2Te_4 when compared with the FM and AFM structures, which needs further verification by neutron scattering experiment. The bifurcation between zero-field-cooling and field-cooling curves [Fig. 3(a)] might be due to strong magnetic anisotropy and/or multidomain structure, which has also been observed in other long-range FM single crystals, such as U_2RhSi_3 [26]. The magnetization loops of FeCr_2Te_4 for both field directions at $T = 2$ K confirm a large magnetic anisotropy and easy c axis [Fig. 3(c)]. The sudden jumps around $\mu_0 H \approx \pm 1$ T along the c axis can be ascribed to the magnetic domain creeping behavior; that is, the magnetic domain walls jump from one pinning site to another. Then we estimated the Rhodes-Wohlfarth ratio (RWR) for FeCr_2Te_4 , which is defined as P_c/P_s , with P_c obtained from the effective moment $P_c(P_c + 2) = P_{\text{eff}}^2$ and P_s being the saturation moment obtained in the ordered state [27–29]. RWR is 1 for a localized system and is larger in an itinerant system. Here we obtain $\text{RWR} \approx 1.69$ for FeCr_2Te_4 , indicating a weak itinerant character. To obtain an accurate Curie temperature T_c , out-of-plane ac susceptibility was measured at an oscillating ac field of 3.8 Oe and a frequency of 499 Hz. The single sharp peak in the real part $m'(T)$ [Fig. 3(d)] gives $T_c = 124$ K.

In the following we discuss the nature of the PM-FIM transition for FeCr_2Te_4 . The magnetization isotherms along the easy c axis were measured at various temperatures in the vicinity of T_c [Fig. 4(a)]. We first considered the well-known Arrott plot [30]. From the Landau theory, the Arrott plot of M^2 vs H/M should appear as parallel straight lines above and below T_c , and the line passes through the origin at T_c . It is clear that the mean-field critical exponent does not work for FeCr_2Te_4 , as illustrated by the set of curved lines in Fig. 4(b).

For a second-order phase transition, the spontaneous magnetization M_s below T_c , the inverse initial susceptibility χ_0^{-1} above T_c , and the field-dependent magnetization $M(H)$ at T_c are [31–33]

$$M_s(T) = M_0(-\varepsilon)^\beta, \quad \varepsilon < 0, T < T_c, \quad (1)$$

$$\chi_0^{-1}(T) = (h_0/m_0)\varepsilon^\gamma, \quad \varepsilon > 0, T > T_c, \quad (2)$$

$$M = DH^{1/\delta}, \quad T = T_c, \quad (3)$$

where $\varepsilon = (T - T_c)/T_c$ is the reduced temperature and M_0 , h_0/m_0 , and D are the critical amplitudes. In a more general case, the modified Arrott plot $(H/M)^{1/\gamma} = a\varepsilon + bM^{1/\beta}$ with the self-consistent method was considered [34,35]. Figure 4(c) presents the final modified Arrott plot of $M^{1/\beta}$ vs $(H/M)^{1/\gamma}$ with $\beta = 0.32$ and $\gamma = 1.21$, showing a set of quasiparallel lines in the high-field region. Then we extracted $\chi_0^{-1}(T)$ and $M_s(T)$ as the intercepts on the H/M axis and the positive M^2 axis, respectively. The magnetic entropy change can be

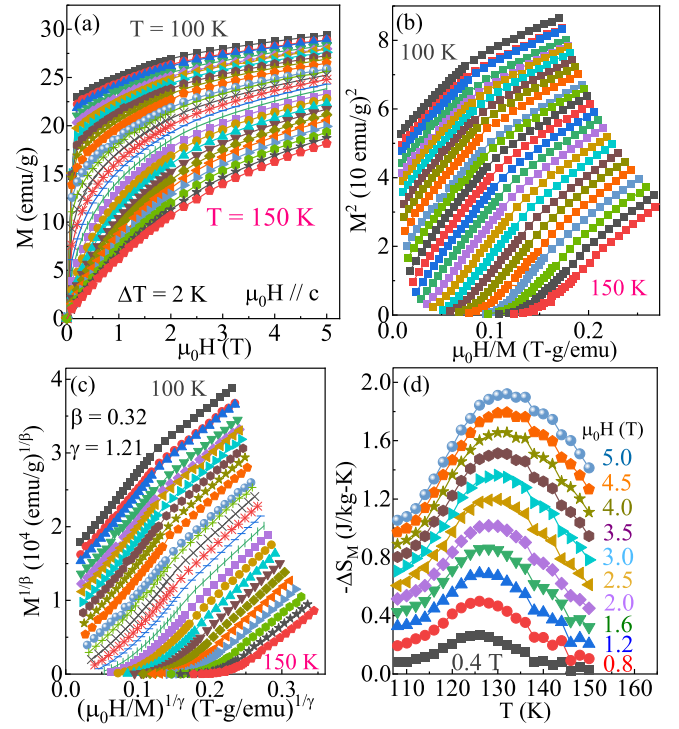


FIG. 4. (a) Typical initial isothermal magnetization curves from 100 to 150 K with a temperature step of 2 K for the FeCr_2Te_4 single crystal. (b) Arrott plot ($\beta = 0.5$, $\gamma = 1$) and (c) the modified Arrott plot with the optimum exponents $\beta = 0.32$ and $\gamma = 1.21$. (d) Temperature-dependent magnetic entropy change $-\Delta S_M(T)$ at various fields.

estimated using Maxwell's relation [36]:

$$\Delta S_M(T, H) = \int_0^H \left[\frac{\partial M(T, H)}{\partial T} \right]_H dH. \quad (4)$$

Figure 4(d) presents the calculated $-\Delta S_M$ as a function of temperature. $-\Delta S_M$ shows a broad peak centered near T_c , and the peak value monotonically increases with increasing field. The maximum value of $-\Delta S_M$ reaches $1.92 \text{ J kg}^{-1} \text{ K}^{-1}$ with a field change of 5 T. There is a slight shift of the $-\Delta S_M$ peak towards higher temperature with increasing field, which also excludes the mean-field model [37].

Figure 5(a) presents the extracted $M_s(T)$ and $\chi_0^{-1}(T)$ as a function of temperature. According to Eqs. (1) and (2), the critical exponents $\beta = 0.33(2)$ with $T_c = 122.9(3)$ K and $\gamma = 1.20(1)$ with $T_c = 122.7(1)$ K are obtained. The exponent β describes the rapid increase of the order parameter below T_c . The exponent γ describes how magnetic susceptibility diverges at T_c . Here the obtained result describes the critical behavior of the net spontaneous magnetization that arises in the ferrimagnet. In the Kouvel-Fisher relation [38]

$$M_s(T)[dM_s(T)/dT]^{-1} = (T - T_c)/\beta, \quad (5)$$

$$\chi_0^{-1}(T)[d\chi_0^{-1}(T)/dT]^{-1} = (T - T_c)/\gamma. \quad (6)$$

Linear fittings to the plots of $M_s(T)[dM_s(T)/dT]^{-1}$ and $\chi_0^{-1}(T)[d\chi_0^{-1}(T)/dT]^{-1}$ in Fig. 5(b) yield $\beta = 0.30(1)$ with $T_c = 122.4(5)$ K and $\gamma = 1.22(1)$ with $T_c = 122.8(1)$ K. The

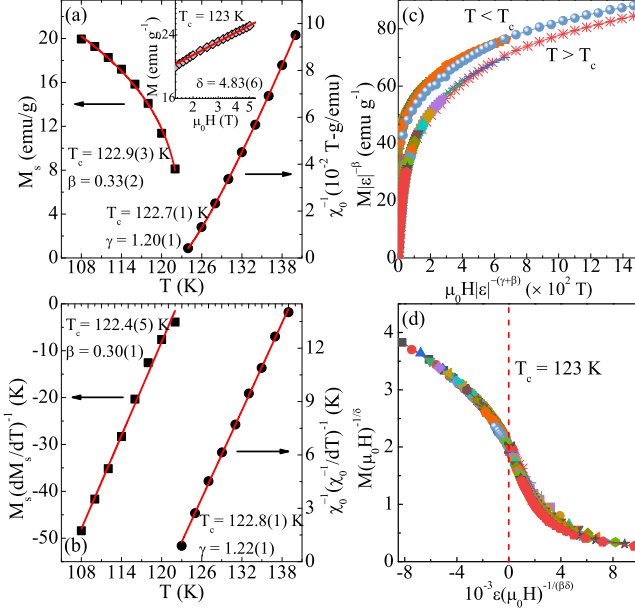


FIG. 5. (a) Temperature dependence of the spontaneous magnetization M_s (left) and the inverse initial susceptibility χ_0^{-1} (right) with solid fitting curves. The inset shows $\log_{10} M$ vs $\log_{10}(\mu_0 H)$ collected at $T_c = 123$ K with a linear fitting curve. (b) Kouvel-Fisher plots of $M_s(dM_s/dT)^{-1}$ (left axis) and $\chi_0^{-1}(d\chi_0^{-1}/dT)^{-1}$ (right axis) with solid fitting curves. (c) Scaled magnetization m vs scaled field h below and above T_c for FeCr_2Te_4 . (d) The rescaling of the $M(\mu_0 H)$ curves by $M(\mu_0 H)^{-1/\delta}$ vs $\epsilon(\mu_0 H)^{-1/(\beta\delta)}$.

third exponent δ can be calculated from the Widom scaling relation $\delta = 1 + \gamma/\beta$ [39]. From β and γ obtained with the modified Arrott plot and the Kouvel-Fisher plot, $\delta = 4.6(2)$ and $5.1(1)$ are obtained, respectively, which are close to the direct fit of $\delta = 4.83(6)$, taking into account that $M = DH^{1/\delta}$ at $T_c = 123$ K [inset in Fig. 5(a)]. The obtained critical exponents of FeCr_2Te_4 are very close to the theoretically predicted values of the 3D Ising model ($\beta = 0.325$, $\gamma = 1.24$, and $\delta = 4.82$; Table II).

A scaling analysis can be used to estimate the reliability of the obtained critical exponents and T_c . The magnetic equation of state in the critical region is expressed as

$$M(H, \epsilon) = \epsilon^\beta f_\pm(H/\epsilon^{\beta+\gamma}), \quad (7)$$

where f_+ for $T > T_c$ and f_- for $T < T_c$, respectively, are the regular functions. Equation (7) can be further written in

terms of scaled magnetization $m \equiv \epsilon^{-\beta} M(H, \epsilon)$ and scaled field $h \equiv \epsilon^{-(\beta+\gamma)} H$ as $m = f_\pm(h)$. This suggests that for true scaling relations and the right choice of β , γ , and δ , scaled m and h will fall on universal curves above T_c and below T_c , respectively. As shown in Fig. 5(c), all the data collapse on two separate branches below and above T_c , respectively. The scaling equation of state takes another form,

$$\frac{H}{M^\delta} = k\left(\frac{\epsilon}{H^{1/\beta}}\right), \quad (8)$$

where $k(x)$ is the scaling function. From the above equation, all the data should also fall onto a single curve. This is, indeed, seen [Fig. 5(d)]; the $M(\mu_0 H)^{-1/\delta}$ vs $\epsilon(\mu_0 H)^{-1/(\beta\delta)}$ experimental data collapse into a single curve, and T_c locates at the zero point of the horizontal axis. The well-rescaled curves confirm the reliability of the obtained critical exponents and T_c .

Furthermore, it is important to discuss the nature as well as the range of magnetic interaction in FeCr_2Te_4 . In a homogeneous magnet the universality class of the magnetic phase transition depends on the exchange distance $J(r)$. In renormalization group theory analysis the interaction decays with distance r as $J(r) \approx r^{-(3+\sigma)}$, where σ is a positive constant [40,41]. The susceptibility exponent γ is

$$\gamma = 1 + \frac{4}{d} \left(\frac{n+2}{n+8} \right) \Delta\sigma + \frac{8(n+2)(n-4)}{d^2(n+8)^2} \times \left[1 + \frac{2G(\frac{d}{2})(7n+20)}{(n-4)(n+8)} \right] \Delta\sigma^2, \quad (9)$$

where $\Delta\sigma = (\sigma - \frac{d}{2})$, $G(\frac{d}{2}) = 3 - \frac{1}{4}(\frac{d}{2})^2$, and n is the spin dimensionality [42]. When $\sigma > 2$, the Heisenberg model is valid for the 3D isotropic magnet, where $J(r)$ decreases faster than r^{-5} . When $\sigma \leq 3/2$, the mean-field model is satisfied, assuming that $J(r)$ decreases slower than $r^{-4.5}$. For the 3D Ising model with $d = 3$ and $n = 1$, $\sigma = 1.88$ is obtained, leading to spin interactions $J(r)$ decaying as $J(r) \approx r^{-4.88}$. This calculation suggests that the spin interaction in FeCr_2Te_4 is close to the 3D Ising localized-type coupled with a long-range ($\sigma = 1.88$) interaction, in line with its weak itinerant character. Meanwhile, the correlation length ξ correlates with the critical exponent ν ($\nu = \gamma/\sigma$), where $\xi = \xi_0[(T - T_c)/T_c]^{-\nu}$. It gives $\nu = 0.64(1)$ and $\alpha = 0.08$ ($\alpha = 2 - \nu d$).

To get further insight into the magnetism, we performed first-principles calculations using density function theory. We applied the WIEN2K implementation [43] of the full-potential

TABLE II. Comparison of critical exponents of FeCr_2Te_4 with different theoretical models.

	Reference	Technique	T_{c-}	T_{c+}	β	γ	δ
FeCr_2Te_4	This work	Modified Arrott plot	122.9(3)	122.7(1)	0.33(2)	1.20(1)	4.6(2)
	This work	Kouvel-Fisher plot	122.4(5)	122.8(1)	0.30(1)	1.22(1)	5.1(1)
	This work	Critical isotherm					4.83(6)
3D Heisenberg	28	Theory			0.365	1.386	4.8
3D XY	28	Theory			0.345	1.316	4.81
3D Ising	28	Theory			0.325	1.24	4.82
Tricritical mean field	36	Theory			0.25	1.0	5.0

TABLE III. The first-principles total energy (in meV) per formula unit of different magnetic patterns as shown in Fig. 6(a) using the 300 and 105 K experimental structures. In the E-AF-2 pattern, a Cr atom is antiferromagnetically and ferromagnetically aligned with the closest and farthest of its six nearest Cr neighbors, respectively; the opposite holds in the E-AF-1 pattern. FM means the ferromagnetic configuration.

Structure	Ferri	FM	C-AF	E-AF-1	E-AF-2
300 K	8	90	197	31	82
105 K	0	56	171	72	32

linearized augmented plane-wave method in the generalized gradient approximation using the PBEsol functional [44]. The basis size was determined by $R_{\text{mt}}K_{\text{max}} = 7$, and the Brillouin zone was sampled with 115 irreducible k points to achieve energy convergence of 1 meV. As shown in Table III, we found that for the experimental structure refined at 105 K, the ferrimagnetic state where the Cr and Fe atoms have opposite spin orientations is 56 meV per formula unit lower in total energy than the ferromagnetic phase and 32 meV lower than the most stable antiferromagnetic structure (i.e., E-AF-2) as observed in FeCr_2Te_4 [45]. A similar trend of the results holds for the experimental structure refined at 300 K (Table III). A weak easy c -axis anisotropy was obtained by inclusion of spin-orbit coupling in the calculations; namely, the total energy per formula unit is lower by less than 1 meV for the magnetization along the c axis than along the a or b axis. Thus, other sources of magnetic anisotropy such as dipole-dipole interaction are important. The calculated atom-resolved density of states (DOS) is shown in Figs. 6(b) and 6(c). For the nonmagnetic case, the Cr-derived DOS has a sharp peak at the Fermi level [Figs. 6(b)], suggesting a strong Stoner instability that yields an itinerant ferromagnetism in the Cr layers. This yields the splitting of about 2.8 eV between the spin-majority and spin-minority bands of Cr character with the dramatic reduction of the Cr-derived DOS at the Fermi level [Fig. 6(c)], indicative of the localized spin picture for the Cr atoms. However, the nonmagnetic Fe-derived DOS peaks at about 0.6 eV below the Fermi level [Fig. 6(b)] and experiences little reduction at the Fermi level upon entering the magnetic phase [Fig. 6(c)]. We infer that the magnetism of the Fe ions is established via antiferromagnetic superexchange with the neighboring two Cr ions. The Cr magnetic moment within the atomic muffin tins is about $2.88\mu_B$, which is close to the nominal Cr^{3+} $S = 3/2$ state. With the octahedral coordination, the splitting of the five $3d$ orbitals between the high-lying e_g and low-lying t_{2g} orbitals is substantial. The $S = 3/2$ state of the Cr^{3+} ion (i.e., the $3d^3$ or $t_{2g}^3e_g^0$ electron configuration) means that the Cr t_{2g} orbitals are half filled, rendering a vanishing orbital angular momentum and a negligible spin-orbit coupling effect. The Fe magnetic moment is about $2.80\mu_B$, significantly deviating from the nominal high-spin Fe^{2+} $S = 2$ state, which indicates its dual character with both localized spins and itinerant electrons. This reveals an interesting interplay of Cr and Fe electronic states, which allows the spin-majority bands of the system at the Fermi level to be of Fe character rather than Cr character [Fig. 6(c)]. We thus picture the FIM in FeCr_2Te_4

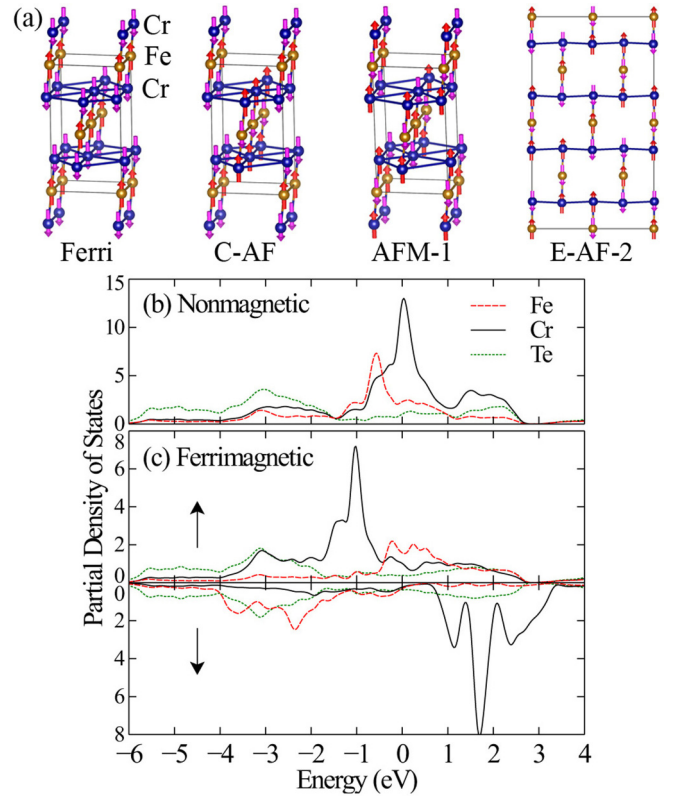


FIG. 6. (a) The antiferromagnetic structures used in the first-principles total energy calculations. Atom-resolved density of states (b) in the nonmagnetic state and (c) in the ferrimagnetic state where the Cr and Fe atoms have opposite spin orientations, which are shown in the ratio of two Cr ions to one Fe ion.

as itinerant ferromagnetism among the antiferromagnetically coupled Cr-Fe-Cr trimers. The trimers centered at the Fe sites form a body-centered orthorhombic lattice of magnetic dipoles with an effective moment of $2\mu_B S = 4\mu_B$ [Fig. 3(c)]. In addition to the effective Heisenberg exchange interaction, the i th trimer is coupled with its ten neighboring trimers [Fig. 6(a)] via dipole-dipole interaction $\propto -(\mathbf{S}_i \cdot \mathbf{r}_{ij})(\mathbf{S}_j \cdot \mathbf{r}_{ij})/|\mathbf{r}_{ij}|^5$, which tends to align the magnetic moments along the bond direction $\mathbf{r}_{ij} = \mathbf{r}_i - \mathbf{r}_j$, where j denotes one of the neighboring trimers and \mathbf{r}_i is the spatial vector of the i th trimer. Since the body-centered orthorhombic structure of the trimers is substantially elongated along the c axis, easy c -axis magnetic anisotropy has the overall minimum deviation from the neighboring bond directions. We thus predict that the 3D Ising-like ferrimagnetism is sensitive to changes in the lattice structure, especially the tilting of the Cr-Fe-Cr trimers, which will be verified by future pressure experiments and computer simulations.

IV. CONCLUSIONS

In summary, we systematically investigated structural and magnetic properties of stoichiometric FeCr_2Te_4 that crystallizes in the $I2/m$ space group. The second-order PM-FIM transition was observed at $T_c \sim 123$ K. The critical exponents β , γ , and δ estimated from various techniques match

reasonably well and follow the scaling equation. The analysis of critical behavior suggests that FeCr_2Te_4 is a 3D Ising system displaying a long-range exchange interaction with the exchange distance decaying as $J(r) \approx r^{-4.88}$. Combined experimental and theoretical analysis attributes the ferrimagnetism in FeCr_2Te_4 to itinerant ferromagnetism among the antiferromagnetically coupled Cr-Fe-Cr trimers. Follow-up studies of local atomic structure and magnetism using x-ray and neutron scattering as well as high-pressure methods will be of particular interest for more comprehensive understanding of this system.

ACKNOWLEDGMENTS

Work at Brookhaven National Laboratory (BNL) is supported by the Office of Basic Energy Sciences, Materials Sciences and Engineering Division, U.S. Department of Energy (DOE) under Contract No. DE-SC0012704. This research used the 28-ID-1 and 8-ID beamlines of the NSLS II, a U.S. DOE Office of Science User Facility operated for the DOE Office of Science by BNL under Contract No. DE-SC0012704. This research used resources of the Center for Functional Nanomaterials (CFN), which is a U.S. DOE Office of Science Facility, at BNL under Contract No. DE-SC0012704.

-
- [1] T. Kanomata, H. Ido, and T. Kaneko, *J. Phys. Soc. Jpn.* **29**, 332 (1970).
- [2] H. W. Lehmann and F. P. Emmenegger, *Solid State Commun.* **7**, 965 (1969).
- [3] N. Menyuk, K. Dwight, and R. J. Arnett, *J. Appl. Phys.* **37**, 1387 (1966).
- [4] Z. R. Yang, S. Tan, Z. W. Chen, and Y. H. Zhang, *Phys. Rev. B* **62**, 13872 (2000).
- [5] V. Tsurkan, M. Mücksch, V. Fritsch, J. Hemberger, M. Klemm, S. Klimm, S. Körner, H. A. Krug von Nidda, D. Samusi, E. W. Scheidt, A. Loidl, S. Horn, and R. Tidecks, *Phys. Rev. B* **68**, 134434 (2003).
- [6] K. Ohgushi, Y. Okimoto, T. Ogasawara, S. Miyasaka, and Y. Tokura, *J. Phys. Soc. Jpn.* **77**, 034713 (2019).
- [7] J. Hemberger, T. Rudolf, H. A. Krug von Nidda, F. Mayr, A. Pimenov, V. Tsurkan, and A. Loidl, *Phys. Rev. Lett.* **97**, 087204 (2006).
- [8] J. Bertinshaw, C. Ulrich, A. Gunter, F. Schrettle, M. Wohlaer, S. Krohns, M. Reehuis, A. J. Studer, M. Avdeev, D. V. Quach, J. R. Groza, V. Tsurkan, A. Loidl, and J. Deisenhofer, *Sci. Rep.* **4**, 6079 (2014).
- [9] V. Tsurkan, O. Zaharko, F. Schrettle, C. Kant, J. Deisenhofer, H. A. Krug von Nidda, V. Felea, P. Lemmens, J. R. Groza, D. V. Quach, F. Gozzo, and A. Loidl, *Phys. Rev. B* **81**, 184426 (2010).
- [10] V. Tsurkan, I. Fita, M. Baran, R. Puzniak, D. Samusi, R. Szymczak, H. Szymczak, S. Klimm, M. Kliem, S. Honn, and R. Tidecks, *J. Appl. Phys.* **90**, 875 (2001).
- [11] A. P. Ramirez, R. J. Cava, and J. Krajewski, *Nature (London)* **386**, 156 (1997).
- [12] B. I. Min, S. S. Baik, H. C. Choi, S. K. Kwon, and J. S. Kang, *New J. Phys.* **10**, 055014 (2008).
- [13] G. J. Snyder, T. Caillat, and J. P. Fleurial, *Phys. Rev. B* **62**, 10185 (2000).
- [14] H. N. Ok and C. S. Lee, *Phys. Rev. B* **33**, 581 (1986).
- [15] J. S. Kang, G. Kim, H. J. Lee, H. S. Kim, D. H. Kim, S. W. Han, S. J. Kim, C. S. Kim, H. Lee, J. Y. Kim, and B. I. Min, *J. Appl. Phys.* **103**, 07D717 (2008).
- [16] A. B. Demeaux, G. Villers, and P. Gibart, *J. Solid State Chem.* **15**, 178 (1975).
- [17] L. M. Valiev, I. G. Kerimov, S. Kh. Babayev, and Z. M. Namazov, *Russ. J. Inorg. Mater.* **11**, 213 (1975).
- [18] C. S. Yadav, S. K. Pandey, and P. L. Paulose, [arXiv:1904.06661](https://arxiv.org/abs/1904.06661).
- [19] E. S. Bozin, W. G. Yin, R. J. Koch, M. Abeykoon, Y. S. Hor, H. Zheng, H. C. Lei, C. Petrovic, J. F. Mitchell, and S. J. L. Billinge, *Nat. Commun.* **10**, 3638 (2019).
- [20] J. Kieffer and J. P. Wright, *Powder Diffr.* **28**, 339 (2013).
- [21] B. H. Toby and R. B. Von Dreele, *J. Appl. Crystallogr.* **46**, 544 (2013).
- [22] A. Ignatov, C. L. Zhang, M. Vannucci, M. Croft, T. A. Tyson, D. Kwok, Z. Qin, and S.-W. Cheong, [arXiv:0808.2134](https://arxiv.org/abs/0808.2134).
- [23] H. Ofuchi, N. Ozaki, N. Nishizawa, H. Kinjyo, S. Kuroda, and K. Takita, *AIP Conf. Proc.* **882**, 517 (2007).
- [24] *X-ray Absorption: Principles, Applications, Techniques of EXAFS, SEXAFS, XANES*, edited by R. Prins and D. C. Koningsberger (Wiley, New York, 1988).
- [25] K. Adachi, K. Sato, and K. Kojima, *Mem. Fac. Eng. Nagoya Univ. Jpn.* **22**, 253 (1970).
- [26] M. Szlawska, M. Majewicz, and D. Kaczorowski, *J. Alloys Compd.* **662**, 208 (2016).
- [27] E. P. Wohlfarth, *J. Magn. Magn. Mater.* **7**, 113 (1978).
- [28] T. Moriya, *J. Magn. Magn. Mater.* **14**, 1 (1979).
- [29] Y. Takahashi, *Spin Fluctuation Theory of Itinerant Electron Magnetism*, Springer Tracts in Modern Physics Vol. 253 (Springer, Berlin, 2013).
- [30] A. Arrott, *Phys. Rev.* **108**, 1394 (1957).
- [31] H. E. Stanley, *Introduction to Phase Transitions and Critical Phenomena* (Oxford University Press, London, 1971).
- [32] M. E. Fisher, *Rep. Prog. Phys.* **30**, 615 (1967).
- [33] J. Lin, P. Tong, D. Cui, C. Yang, J. Yang, S. Lin, B. Wang, W. Tong, L. Zhang, Y. Zou, and Y. Sun, *Sci. Rep.* **5**, 7933 (2015).
- [34] W. Kellner, M. Fähnle, H. Kronmüller, and S. N. Kaul, *Phys. Status Solidi B* **144**, 387 (1987).
- [35] A. K. Pramanik and A. Banerjee, *Phys. Rev. B* **79**, 214426 (2009).
- [36] J. Amaral, M. Reis, V. Amaral, T. Mendonc, J. Araujo, M. Sa, P. Tavares, and J. Vieira, *J. Magn. Magn. Mater.* **290**, 686 (2005).
- [37] V. Franco, A. Conde, M. D. Kuzmin, and J. M. Romero-Enrique, *J. Appl. Phys.* **105**, 07A917 (2009).
- [38] J. S. Kouvel and M. E. Fisher, *Phys. Rev.* **136**, A1626 (1964).
- [39] B. Widom, *J. Chem. Phys.* **41**, 1633 (1964).
- [40] S. Kaul, *J. Magn. Magn. Mater.* **53**, 5 (1985).
- [41] M. E. Fisher, S. K. Ma, and B. G. Nickel, *Phys. Rev. Lett.* **29**, 917 (1972).
- [42] S. F. Fischer, S. N. Kaul, and H. Kronmüller, *Phys. Rev. B* **65**, 064443 (2002).
- [43] K. Schwarz, P. Blaha, and G. K. H. Madsen, *Comput. Phys. Commun.* **147**, 71 (2002).
- [44] J. P. Perdew, A. Ruzsinszky, G. I. Csonka, O. A. Vydrov, G. E. Scuseria, L. A. Constantin, X. Zhou, and K. Burke, *Phys. Rev. Lett.* **100**, 136406 (2008).
- [45] S. R. Hong and H. N. Ok, *Phys. Rev. B* **11**, 4176 (1975).